

A new quantum clock for measuring photoemission delay times

Daehyun You¹, Kiyoshi Ueda^{1,*}, Elena V. Gryzlova², Alexei N. Grum-Grzhimailo², Maria M. Popova³, Ekaterina I. Staroselskaya³, Oyunbileg Tugs⁴, Yuki Orimo⁴, Takeshi Sato^{4,5,6}, Kenichi L. Ishikawa^{4,5,6}, Paolo Antonio Carpeggiani⁷, Tamás Csizmadia⁸, Miklós Füle⁸, Giuseppe Sansone⁹, Praveen Kumar Maroju⁹, Alessandro D'Elia¹⁰, Tommaso Mazza¹¹, Michael Meyer¹¹, Carlo Callegari¹², Michele Di Fraia¹², Oksana Plekan¹², Robert Richter¹², Luca Giannessi^{12,13}, Enrico Allaria¹², Giovanni De Ninno^{12,14}, Mauro Trovò¹², Laura Badano¹², Bruno Diviacco¹², David Gauthier^{12,15}, Najmeh Mirian¹², Giuseppe Penco¹², Primož Rebernik Ribič¹², Simone Spampinati¹², Carlo Spezzani¹², Giulio Gaio¹², and Kevin C. Prince^{12,16,*}

¹ Institute of Multidisciplinary Research for Advanced Materials, Tohoku University, Sendai 980-8577, Japan

² Skobeltsyn Institute of Nuclear Physics, Lomonosov Moscow State University, Moscow 119991, Russia

³ Faculty of Physics, Lomonosov Moscow State University, Moscow 119991, Russia

⁴ Department of Nuclear Engineering and Management, Graduate School of Engineering, The University of Tokyo, 7-3-1 Hongo, Bunkyo-ku, Tokyo 113-8656, Japan

⁵ Photon Science Center, Graduate School of Engineering, The University of Tokyo, 7-3-1 Hongo, Bunkyo-ku, Tokyo 113-8656, Japan

⁶ Research Institute for Photon Science and Laser Technology, The University of Tokyo, 7-3-1 Hongo, Bunkyo-ku, Tokyo 113-0033, Japan

⁷ Institut für Photonik, Technische Universität Wien, 1040 Vienna, Austria

⁸ ELI-ALPS, ELI-HU Non-Profit Ltd., Dugonics tér 13, H-6720 Szeged, Hungary

⁹ Physikalisches Institut, Universität Freiburg, 79106 Freiburg, Germany

¹⁰ University of Trieste, Department of Physics, 34127 Trieste, Italy

¹¹ European X-Ray Free Electron Laser Facility GmbH, Holzkoppel 4, 22869 Schenefeld, Germany

¹² Elettra-Sincrotrone Trieste, 34149 Basovizza, Trieste, Italy

¹³ ENEA C.R. Frascati, 00044 Frascati, Rome, Italy

¹⁴ Laboratory of Quantum Optics, University of Nova Gorica, Nova Gorica 5001, Slovenia

¹⁵ Now at LIDYL, CEA, CNRS, Université Paris-Saclay, CEA-Saclay, 91191 Gif-sur-Yvette, France.

¹⁶ Centre for Translational Atomaterials, Swinburne University of Technology, Melbourne, Australia

*Corresponding authors: kiyoshi.ueda@tohoku.ac.jp, prince@elettra.eu

In photoionization, the extremely short delay between photon annihilation and electron emission is known as the Eisenbud-Wigner-Smith (EWS) delay, and is usually measured in attoseconds (10^{-18} seconds). We present a new method for measuring this delay, together with experimental results and theoretical calculations. We use two phase-locked Extreme Ultraviolet pulses of frequency ω and 2ω , from a Free-Electron Laser. This technique avoids the use of the infrared field required by current methods of measuring EWS delays, eliminating the need for corrections of the experimental data due to the IR field. Relative phases between one- and two-photon ionization channels are extracted, and are independent of photoelectron amplitudes. We derived the relative EWS delay for one- and two-photon ionization of neon as a function of emission angle.

The age of attosecond physics was ushered in by the invention of methods for probing samples on a time scale less than femtoseconds (*1*), and currently many ultrafast phenomena are being investigated. Photoemission is one such process which has attracted much interest, particularly regarding the time delay between the absorption of a photon and the emission of a photoelectron, known as the Eisenbud-Wigner-Smith (EWS) time delay (*2*). For many years, photoemission was approximated as a process in which an electron was ejected instantaneously by a photon because no methods were available to probe the process on the attosecond scale.

Now that techniques exist (3), theories can be tested directly, and great theoretical and experimental interest has been stimulated (4–9).

There are currently two chief methods of measuring the EWS time delay. In attosecond streaking (3), an ultrafast, short-wavelength pulse initiates the emission of an electron, and a femtosecond infrared (IR) pulse acts as a streaking field, by changing the linear momentum of the electron (as in a streak camera). A variant of this method is the attosecond clock technique (10–13), in which circular polarization is used to measure tunneling ionization times. The second main technique for measuring EWS delays is interferometric, and is known as RABBITT (Reconstruction of Attosecond Beating By Interference of Two-photon Transitions): it uses a train of attosecond pulses dressed by a phase-locked IR pulse (14). The requirements on the pulse durations are relaxed in this case; for example, IR pulses of 30 fs duration and pulse trains of comparable length may be used (7). Usually the IR pulse is the fundamental of the odd harmonics in the pulse train, although Loriot *et al.* (15) reported a variant in which the dressing field was the second harmonic of the fundamental, and angle-resolved detection was used. As well as these methods, recent work on phase retrieval includes a method based on photo-recombination (16), and two-colour, two-photon ionization via a resonance (17).

Streaking, RABBITT and the last mentioned techniques depend on the extreme temporal precision with which an IR pulse can be synchronized with a short-wavelength pulse or pulse train. The latter is generated by HHG conversion of part of the light from the same source as the IR. Although the IR field is relatively weak for streaking and RABBITT, it generally perturbs the results of both methods, so that it is necessary to apply corrections during analysis, and maintain a sufficiently low IR power. The additional correction to the EWS delay is termed Coulomb-laser coupling shift, in the case of attosecond streaking, and continuum-continuum coupling shift in the case of RABBITT (2). To date, all such corrections have been made on the basis of theoretical calculations, and no measurements are available to test their accuracy.

Pazourek *et al.* (2) have labelled streaking techniques “classical clocks”, as they depend only on classical fields, and interferometric methods “quantum clocks” as they depend on the wave nature of matter, as well as that of light. With few exceptions (18), measurements are of relative time delays, for example emission from two different levels of the same atom (5), or from two different targets measured simultaneously (6) or sequentially (8).

The EWS delay depends on the kinetic energy of the photoelectron, and also on its direction of emission. For the case of isotropic initial and final ionic states, the delay is isotropic, but where the photoelectron wave packet consists of two or more partial waves, interference gives rise to angular dependence (19). There has been significant theoretical work on the angle-dependent time delay, for example (20–23), but few related experimental reports (19, 24, 25), all three using the RABBITT technique. Even though the delay was expected to be isotropic for one-photon ionization of He, Heuser *et al.* (19) observed an angular dependence at some angles, attributed to the effect of the IR pulse, which is necessary for the RABBITT interferometry.

The EWS delay is expressed as

$$\tau(E_k) = \frac{\partial \eta}{\partial E_k} \quad (1)$$

where τ is the angle-dependent electron wave packet group delay, η is the phase of the outgoing electron wave packet and the kinetic energy of the electron wave packet, and $E_k =$ energy of the ionizing photon or photons minus the ionization potential of the target.

In the present work, we demonstrate a method of measuring the EWS delay that does not require an IR pulse. Using only fundamental wavelengths and their second harmonics, we measure angular distributions of photoelectrons emitted from neon to determine the phase relationships for one- and two-photon ionization. By analysing this data, we clock the angular dependence of the difference in EWS delay for electrons emitted by single- and two-photon processes.

Results

Our method is based on the use of short wavelength XUV light, consisting of phase-locked first and second harmonics. This method eliminates the perturbation of the IR field present in the streaking and RABBITT approaches. Furthermore, being interferometric, our technique does not require extremely short, few-cycle pulses, such as those needed for streaking, but it depends instead on extremely accurate phase control (a few attoseconds). Such fine control is available from the Free-Electron Laser FERMI (26).

The technique utilizes a bichromatic beam, consisting of a fundamental wavelength and its temporally overlapping second harmonic, which irradiate a sample (27), shown schematically in Fig. 1. The highly intense fundamental radiation causes two-photon ionization, while the weak second harmonic gives rise to one-photon ionization. The energy of the photoelectrons created coherently in the two channels is identical, so that electrons with the same linear momentum interfere (17). The photoelectron angular distribution (PAD) is measured, and the wavelength is then changed and the measurement repeated. From the difference in phases and electron energies at the two wavelengths, the derivative of the phase, Eq. (1), is calculated, thus yielding the EWS time delay.

The sample consisted of a mixture of helium and neon. In other experiments (6, 8), use of two gases allowed referencing of the photoionization delay time of one electron to that of another. In the present case, we used the admixture of helium to correct for phase offsets introduced when the photon energy was changed (28). Further detailed experimental conditions are in the Supplementary Materials, Materials and Methods section.

The linearly polarized electric field is described by:

$$E(t) = \sqrt{I_{\omega}(t)} \cos \omega t + \sqrt{I_{2\omega}(t)} \cos (2\omega t - \phi). \quad (2)$$

where ω and 2ω are the angular frequencies of the first and second harmonic; $I_{\omega}(t)$ and $I_{2\omega}(t)$

are the envelopes of the two pulses, ϕ denotes the ω - 2ω relative phase (the larger ϕ , the more delayed the 2ω pulse).

We measured the PAD $I(\theta)$ at each optical phase ϕ , where θ is the polar angle from the polarization axis. The photoelectron intensity at a given angle oscillates when the optical phase ϕ is scanned, as indicated in Figs. 2A and 2B:

$$I(\theta; \phi) = A_0(\theta) + A(\theta) \cos(\phi - \Delta\eta(\theta)), \quad (3)$$

where $\Delta\eta(\theta)$ is the difference between the two-photon ionization phase and the one-photon ionization phase at each polar angle θ . Note that the curves in Figs. 2A and 2B oscillate in antiphase, because they correspond to emission directions on opposite sides of the photon propagation direction. The theoretical descriptions of $I(\theta; \phi)$ and $\Delta\eta(\theta)$ are given in the Supplementary Material. We extracted $\Delta\eta(\theta)$ at three combinations of ω and 2ω corresponding to photoelectron kinetic energies, 7.0 eV, 10.2 eV and 16.6 eV, at each polar angle, from the measured PADs, assuming the symmetry $\Delta\eta(\theta) = \Delta\eta(\pi - \theta) + \pi$, as shown in Figs. 2C–2E. One can see a significant increase of $\Delta\eta(\theta)$ at $\sim 90^\circ$, especially at 10.2 eV. The angular dependent variations of $\Delta\eta(\theta)$ at 7.0 eV and 16.6 eV are similar. We have performed calculations for the phase shift differences $\Delta\eta(\theta)$ within the perturbation theory and by real time *ab initio* methods. The details of these calculations are given in the Supplementary Material. Both theories reproduce well the observed behavior as seen in Figs. 2C–2E.

Figure 3 shows the dependence of $\Delta\eta(\theta)$ on electron kinetic energy and polar angle θ , calculated by perturbation theory. The behavior of $\Delta\eta$ in the region of the resonance is complicated: we can clearly see that $\Delta\eta(\theta)$ at $\theta \sim 90^\circ$ increases near the resonance of the fundamental wavelength, ($2p \rightarrow 3s$) at 12.0 eV (kinetic energy for two-photon ionization) and then comes back to the level close to the lower energy values at ~ 7 eV. This clearly illustrates that the large phase shift difference observed at 10.2 eV in Fig. 2D is due to the influence of the resonance at

12.0 eV (23, 24).

The variation of $\Delta\eta(\theta)$ below the resonance is smooth and so we can estimate the difference $\Delta\tau(\theta)$ in the EWS delay of two-photon ionization relative to one-photon ionization, employing the two energy points at 7.0 eV and 10.2 eV and assuming linear energy dependence between these kinetic energies. In Fig. 4, the experimental values of $\Delta\tau(\theta)$ at each polar angle θ are compared with the two theoretical values calculated from $\Delta\eta(\theta)$ at 7.0 eV and 10.2 eV. The observed EWS delay difference is almost zero in the direction parallel to the polarization vector, while it is significant in the perpendicular direction; two-photon ionization is ~ 230 attoseconds slower than one-photon ionization at the average energy of 8.6 eV. This behavior is well reproduced by both theories, and in particular, the time-dependent *ab initio* method exhibits excellent agreement with the experiment, validating the present experimental method. The energy-dependent variation of $\Delta\tau(\theta)$ was also studied using perturbation theory and the results are shown in the Supplementary Materials.

We show in the Supplementary Material that the method is independent of the relative intensities of the fundamental and second harmonic radiation, see Eqs. (S14) to (S22). This is a considerable advantage from an experimental point of view, as it is not necessary to measure precisely the intensity and focal spot shape. Furthermore, there are no effects due to volume averaging over the Gaussian spot profile, or over the duration of the pulses. We verified this experimentally for the kinetic energy of 10.2 eV, Fig. 2D, where the ratio of ionization rates was 1:4 (rather than 1:2 used for the other energies), and the experiment and theory agree well.

In this work we have described a new method to determine angle-resolved EWS time delay, and used it to measure the difference in delays between one- and two-photon ionization. Since the method is based on FEL radiation it can be extended to shorter wavelengths, eventually reaching the core levels, which lie in a wavelength region where optical lasers have reduced pulse energy. This is an important addition to the armoury of techniques available to attosec-

ond science, gives access to the EWS delay for two-photon transitions, and is applicable to molecules as well as atoms. It does not suffer from artifacts due to the presence of an IR pulse, which is necessary for angle-resolved RABBITT and streaking (29). Since no IR is required, the data does not need to be corrected.

References

1. F. Krausz, M. Ivanov, *Rev. Mod. Phys.* **81**, 163 (2009).
2. R. Pazourek, S. Nagele, J. Burgdörfer, *Rev. Mod. Phys.* **87**, 765 (2015).
3. M. Schultze, *et al.*, *Science* **328**, 1658 (2010).
4. S. Pabst, J. M. Dahlström, *Phys. Rev. A* **94**, 1 (2016).
5. K. Klünder, *et al.*, *Phys. Rev. Lett.* **106**, 1 (2011).
6. D. Guénot, *et al.*, *J. Phys. B* **47**, 245602 (2014).
7. D. Guénot, *et al.*, *Phys. Rev. A* **85**, 053424 (2012).
8. C. Palatchi, *et al.*, *J. Phys. B* **47**, 245003 (2014).
9. A. S. Kheifets, *Phys. Rev. A* **87**, 063404 (2013).
10. P. Eckle, *et al.*, *Science* **322**, 1525 (2008).
11. P. Eckle, *et al.*, *Nat. Phys.* **4**, 565 (2008).
12. A. N. Pfeiffer, *et al.*, *Nat. Phys.* **8**, 76 (2012).
13. A. N. Pfeiffer, C. Cirelli, M. Smolarski, R. Dörner, U. Keller, *Nat. Phys.* **7**, 428 (2011).
14. P. M. Paul, *et al.*, *Science* **292**, 1689 (2001).

15. V. Lorient, *et al.*, *J. Opt.* **19**, 114003 (2017).
16. D. Azoury, *et al.*, *Nat. Photonics* **13**, 198 (2019).
17. D. M. Villeneuve, P. Hockett, M. J. J. Vrakking, H. Niikura, *Science* **356**, 1150 (2017).
18. M. Ossiander, *et al.*, *Nature* **561**, 374377 (2018).
19. S. Heuser, *et al.*, *Phys. Rev. A* **94**, 063409 (2016).
20. A. Mandal, P. C. Deshmukh, A. S. Kheifets, V. K. Dolmatov, S. T. Manson, *Phys. Rev. A* **96**, 1 (2017).
21. I. A. Ivanov, A. S. Kheifets, *Phys. Rev. A* **96**, 013408 (2017).
22. A. W. Bray, F. Naseem, A. S. Kheifets, *Phys. Rev. A* **98**, 043427 (2018).
23. S. Banerjee, P. C. Deshmukh, V. K. Dolmatov, S. T. Manson, A. S. Kheifets, *Phys. Rev. A* **99**, 013416 (2019).
24. C. Cirelli, *et al.*, *Nat. Comm.* **9**, 955 (2018).
25. J. Vos, *et al.*, *Science* **360**, 1326 (2018).
26. K. C. Prince, *et al.*, *Nat. Photonics* **10**, 176 (2016).
27. M. Shapiro, P. Brumer, *Principles of the Quantum Control of Molecular Processes* (Wiley-Interscience, 2003).
28. M. Di Fraia *et al.*, submitted for publication.
29. H. Wei, T. Morishita, C. D. Lin, *Phys. Rev. A* **93**, 053412 (2016).

Acknowledgments

We thank the machine physicists of FERMI for making this experiment possible by their excellent work in providing high quality FEL light.

Funding. This work was supported in part by the X-ray Free Electron Laser Utilization Research Project and the X-ray Free Electron Laser Priority Strategy Program of the Ministry of Education, Culture, Sports, Science, and Technology of Japan (MEXT) and the IMRAM program of Tohoku University, and the Dynamic Alliance for Open Innovation Bridging Human, Environment and Materials program. DY wishes to thank supports by JSPS KAKENHI Grant Number JP19J12870, and a Grant-in-Aid of Tohoku University Institute for Promoting Graduate Degree Programs Division for Interdisciplinary Advanced Research and Education. EVG, EIS and MMP acknowledge the Foundation for the Advancement of Theoretical Physics and Mathematics “BASIS.” KLI gratefully acknowledges support by the Cooperative Research Program of the “Network Joint Research Center for Materials and Devices (Japan),” Grant-in-Aid for Scientific Research (Grants No. 16H03881, No. 17K05070, No. 18H03891, and No. 19H00869) from MEXT, the Photon Frontier Network Program of MEXT, the Center of Innovation Program from the Japan Science and Technology Agency, JST, CREST (Grant No. JPMJCR15N1), JST, Quantum Leap Flagship Program of MEXT, and Japan-Hungary Research Cooperative Program, JSPS and HAS. MM and TM acknowledge support by the Deutsche Forschungsgemeinschaft (DFG) under Grant No. SFB925/1. We acknowledge the support of the Italian Ministry of Research Project FIRB No. RBID08CRXK and No. PRIN 2010 ERFKXL 006, the bilateral project CNR JSPS Ultrafast science with extreme ultraviolet Free Electron Lasers, and funding from the European Union Horizon 2020 research and innovation program under the Marie Skłodowska-Curie Grant Agreement No. 641789 MEDEA (Molecular ElectronDynamics investigated by IntenseE Fields and Attosecond Pulses).

Author contributions. KU and KCP conceived and designed the experiment, wrote the proposal FERMI no. 20144077 which gained approval of the beamtime, and supervised the running of the experiment. CC, MDF, OP, DY, KU, PAC, TC, GS, PKM, ADE, KCP, MF, TM, MM, and RR participated in the experiment (operation of experimental station, acquisition of data, preliminary analysis, etc.), and LG, EA, GDN, MT, LB, BD, DG, NM, GP, PRR, SS, CS, GG participated in the experiment by operating the light source. KU and DY performed the detailed analysis of the experimental data. DY, KU, KLI, OT, YO, TS, EVG, MMP, EIS and ANGG analysed the theoretical description of the experiment and carried out calculations. KU and KCP drafted the manuscript, which was then reviewed and edited together with DY, KLI, ANGG and EVG, and circulated to all authors to obtain their input.

Competing interests. The Authors declare no competing interests.

Data and materials availability. All data needed to evaluate the conclusions in the paper are present in the paper or the supplementary materials. The code used to analyse the data is available at https://github.com/DaehyunPY/FERMI_20144077.

Supplementary Materials

Materials and Methods

Supplementary Text

Eq. (S1-S34)

Fig. S1

Table S1

References (30-51)

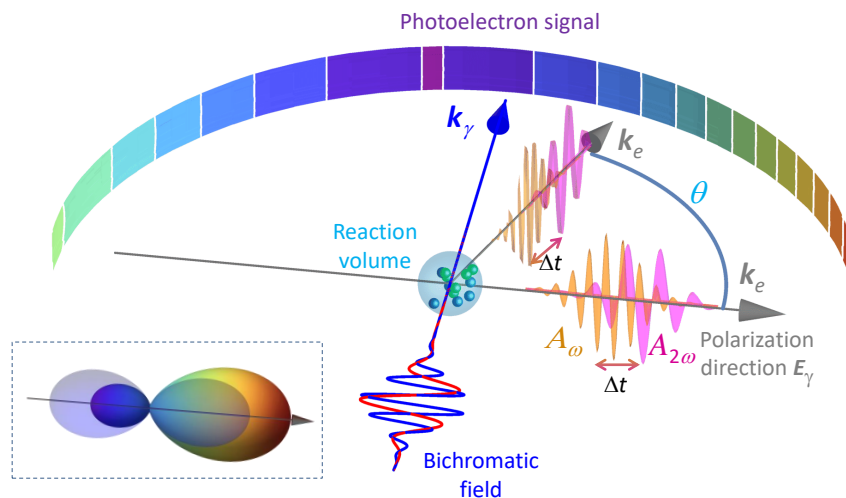


Fig. 1. Scheme of the experiment: bichromatic, linearly polarized light, with momentum k_γ and electric vector E_γ , ionizes neon in the reaction volume. A_ω and $A_{2\omega}$ indicate the amplitudes of photoelectron wave packets produced by the fundamental and second harmonic, respectively, and k_e is the electron momentum. The time delay Δt between the amplitudes depends on emission angle; interference of two amplitudes leads to different electron signals for different angles. Inset, lower left: polar plot of photoelectron intensity at $E_k = 16.6$ eV for coherent harmonics (colored) and incoherent harmonics (grey).

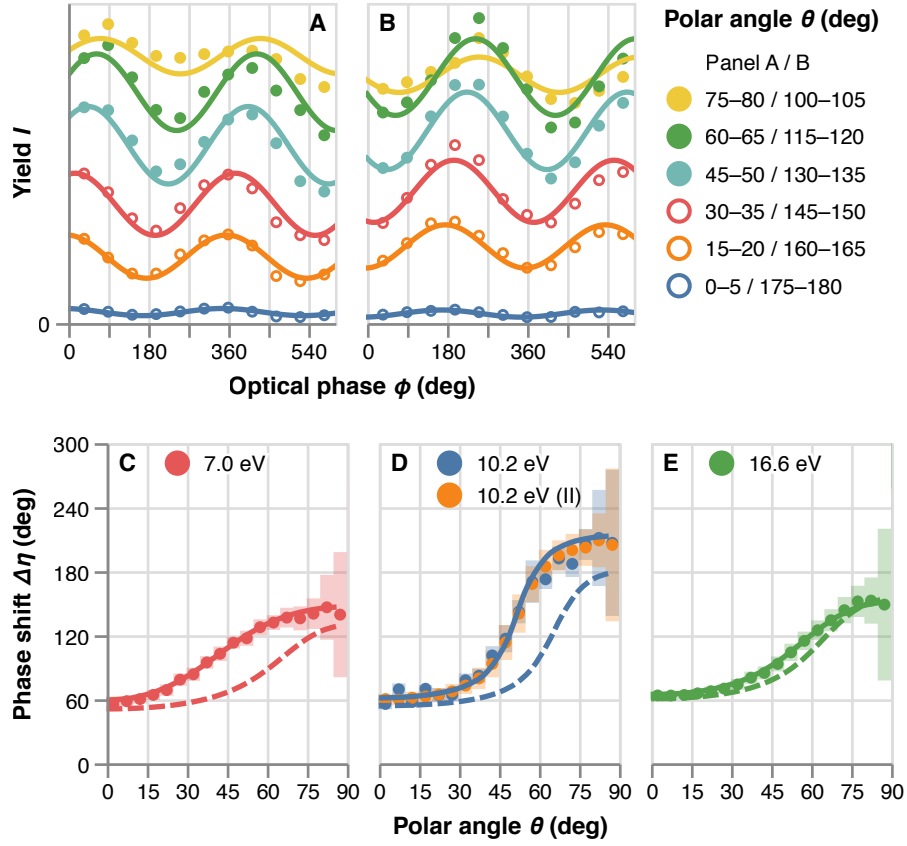


Fig. 2. Upper panels: typical photoelectron yields $I(\theta; \phi)$ as a function of optical phase ϕ at different polar angles θ . The signal was integrated over the 5° intervals shown on the right. The photoelectron kinetic energy is 7.0 eV. Circles are experimental results; lines are sinusoidal fits of the experimental results. Lower panels: extracted phase shift differences as a function of the polar angles, for four data sets and three photoelectron kinetic energies. Left (C), 7.0 eV; middle (D), 10.2 eV; right (E) 16.6 eV. Circles are experimental results; shaded areas show their uncertainties. Dashed lines: perturbation theory; solid lines: real time *ab initio* theory.

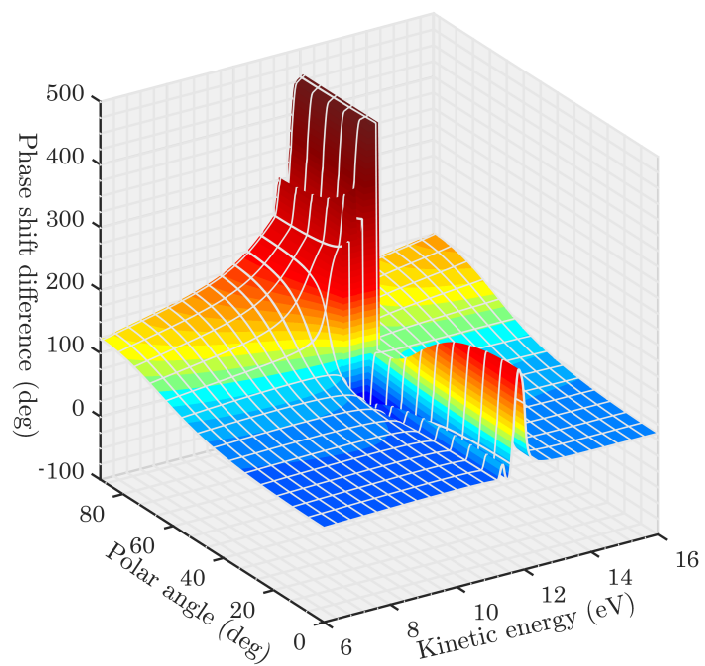


Fig. 3. Phase shift differences $\Delta\eta(\theta)$, calculated by perturbation theory, as a function of the polar angle θ and photoelectron kinetic energy. A large variation near 12.0 eV kinetic energy is due to the $2p \rightarrow 3s$ resonance.

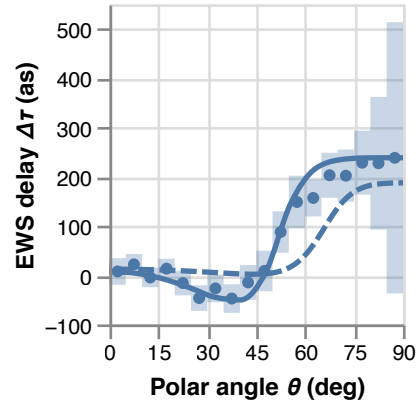


Fig. 4. EWS delay differences $\Delta\tau(\theta)$ of the two-photon ionization relative to the one-photon ionization. Theory and experiment, both estimated from two photoelectron energies 7.0 eV and 10.2 eV, are compared in the figure. Circles are experimental results; shaded areas show their uncertainties. Dashed line: result from perturbation theory; solid lines: result from the real time *ab initio* method.

Supplementary Materials for A new quantum clock for measuring photoemission delay times

Introduction

In the following sections, we give details of the experimental parameters and methods, the theoretical calculations, and the data analysis.

Materials and Methods

The experimental methods have been described elsewhere (26) and are summarized here briefly. The experiment was carried out at the Low Density Matter Beamline (30, 31), using the Velocity Map Imaging spectrometer installed there. The relative phase of the two wavelengths was controlled by means of the electron delay line or phase shifter (32) used previously. It has been calculated that the two pulses have good temporal overlap with slightly different durations and only a small mean variation of the phase within the Full Width at Half Maximum of the pulses, for example 0.07 rad for a fundamental photon energy of 18.5 eV (26).

The intensities of the two wavelengths for the experiments were set as follows. With the last undulator open (that is, inactive), the first harmonic from the first five undulators was set to a chosen wavelength. A small amount of incoherent second harmonic radiation (intensity of the order 1% of the fundamental) is produced by the undulators (33), and to absorb this, the

gas filter available at FERMI was filled with helium. Helium is transparent at all of the fundamental wavelengths used in this study. The two-photon photoelectron signal from the neon and helium gas sample was observed with the VMI spectrometer. The last undulator was then closed to produce the second harmonic and the photoelectron spectrum of the combined beams was observed. The helium gas pressure in the gas cell was then adjusted to achieve a ratio of the ionization rates due to two-photon and one-photon ionization of 1:2 for kinetic energies of 7.0 and 10.2 eV. For the kinetic energy of 15.9 eV, the ratio was 1:4. The bichromatic beam was focused by adjusting the curvature of the Kirkpatrick-Baez active optics (34), and verified experimentally by measuring the focal spot size of the second harmonic with a Hartmann wavefront sensor. This instrument was not able to measure the spot size of the beams at the fundamental wavelengths, so it was calculated (35). The measured spot was elliptical with a size $(4.5 \pm 1) \times (6.5 \pm 1) \mu\text{m}^2$ (FWHM), and the estimated pulse duration was 100 fs.

The average pulse energies of the first harmonics at the exit of the undulators are given in Table S1, together with the kinetic energy of the electrons emitted via single-photon (2ω) or two-photon ($\omega + \omega$) ionization. The estimate of the pulse energy at 14.3 eV was indirect, since the gas cell monitors do not function at this energy, because they are based on ionization of nitrogen gas, and the photon energy is below the threshold for ionization. The approach was to first use the in-line spectrometer (36) to measure spectra at 15.9 eV energy and simultaneously the pulse energies from the gas cell monitors, which gave a calibration of the spectrometer intensity versus pulse energy at this wavelength. Then spectrometer spectra were measured at 14.3 eV, and corrected for grating efficiency and detector sensitivity, to yield pulse energies. The pulse energies at the end-station were calculated by multiplying the values at the exit from the undulators by the transmission of the beamline (31). Using the above spot sizes and pulse durations, the average irradiance at the sample was calculated, Table S1.

The atomic beam was produced by a supersonic expansion and defined by a skimmer and

vertical slits. The length of the beam along the light propagation direction was approximately 1 mm. The VMI data was analyzed using the BASEX method (37), which utilises an Abel transform to generate the Photoelectron Angular Distribution.

The sample consisted of a mixture of helium and neon. In other experiments (52, 53), use of two gases allowed referencing of the photoionization delay time of one electron to that of another. In the present case, we used the admixture of helium to resolve a technical problem: when the Free-Electron Laser wavelength is changed, the mechanical settings of the magnetic structures (undulators) creating the light are changed. This may introduce an unknown phase error between fundamental and second harmonic light. We have shown elsewhere that the PAD of helium $1s$ electrons can be used to determine the absolute phase, with input of only few theoretical parameters (54), and so helium was used as a reference.

Angle-resolved wave packet time delay

We describe the electron wave packet sufficiently far away from the origin (the neon nucleus) in a given direction $\{\theta, \varphi\}$ as

$$\int_0^\infty c(\epsilon) e^{-i\epsilon t} e^{i(\sqrt{2\epsilon}r + \eta(\epsilon))} d\epsilon, \quad (\text{S1})$$

where ϵ is the photoelectron kinetic energy, $c(\epsilon)$ the real-valued amplitude, $\eta(\epsilon)$ the phase. We use Hartree atomic units unless otherwise stated. The group delay, interpreted as photoemission delay or time delay of this wave packet, is given by $\partial\eta(\epsilon)/\partial\epsilon$ (similar to the group delay of a laser pulse).

We consider here the wave packet created by the ω - 2ω electric field described by Equation (2) in the main text. In the ω - 2ω process, the wave packet is expressed as

$$\int_0^\infty e^{-i\epsilon t} e^{i\sqrt{2\epsilon}r} (c_\omega(\epsilon)e^{i\eta_\omega(\epsilon)} + c_{2\omega}(\epsilon)e^{i(\eta_{2\omega}(\epsilon)+\phi)}) d\epsilon. \quad (\text{S2})$$

The group delay of the one-photon and two-photon ionizations can be defined as $\partial\eta_\omega(\epsilon)/\partial\epsilon$ and $\partial\eta_{2\omega}(\epsilon)/\partial\epsilon$, respectively. The photoionization yield as a function of ϕ is given by

$$\begin{aligned} I(\phi) &= \int_0^\infty c_\omega(\epsilon)^2 + c_{2\omega}(\epsilon)^2 + 2c_\omega(\epsilon)c_{2\omega}(\epsilon) \cos(\phi - \Delta\eta(\epsilon)) d\epsilon \\ &\approx A_0 + A \cos(\phi - \Delta\eta(E_k)), \end{aligned} \quad (\text{S3})$$

where E_k is the average kinetic energy of the wave packet, and $\Delta\eta(\epsilon) \equiv \eta_\omega(\epsilon) - \eta_{2\omega}(\epsilon)$ is the phase of two-photon ionization relative to the one-photon ionization. Then,

$$\Delta\tau = \frac{\partial\Delta\eta(E_k)}{\partial E_k}, \quad (\text{S4})$$

can be considered as the delay difference between the two-photon and one-photon ionization wave packets.

This treatment may be generalized to the case of a few wave packets. In particular, expressing the photoionization yield as in Eq. (S3)

$$I(\phi) = A_0 + A \cos(\phi - \Delta\eta) = \sum_m A_{0,m} + A_m \cos(\phi - \Delta\eta_m), \quad (\text{S5})$$

where summation is over the wave packets. This leads to

$$A_0 = \sum_m A_{0,m}, \quad A \cos(\phi - \Delta\eta) = \sum_m A_m \cos(\phi - \Delta\eta_m). \quad (\text{S6})$$

The second equation can be viewed as the definition of the *average* $\Delta\eta$ of $\{\Delta\eta_m\}$.

Perturbation theory

In the experiment, the number of optical cycles in the pulse is of the order of 400 for the fundamental and therefore we can treat the field as having constant amplitude and omit the initial phase of the field with respect to the envelope (carrier-envelope phase). Within the perturbation theory, we checked that our final results with an envelope including 100 optical cycles or more

differ only within the optical linewidth from those obtained with the constant amplitude field. Thus, we describe the bichromatic electric field as

$$E(t) = F_0 (\cos \omega t + k \cos(2\omega t - \phi)) . \quad (\text{S7})$$

Furthermore, we make three assumptions: the dipole approximation for the interaction of the atom with the classically described electromagnetic field, the validity of the lowest nonvanishing order perturbation theory with respect to this interaction, and the LS-coupling approximation within the independent particle model for description of the atomic (ionic) structure. These approximations are well fulfilled for neon in the FEL spectral range and intensities of interest here. With these approximations, the photoelectron angular distribution $I(\theta, \varphi)$ of a Ne $2p$ electron can be derived by standard methods (38) in the form

$$I(\theta, \varphi) = I_0 \sum_{m=0, \pm 1} \left| \sum_{\xi} C_{\xi}^m(\phi) Y_{\ell_{\xi} m}(\theta, \varphi) \right|^2 , \quad (\text{S8})$$

where m is the magnetic quantum number of the initial $2p$ electron, $Y_{\ell m}(\theta, \varphi)$ is a spherical harmonic in the Condon-Shortley phase convention, I_0 is a normalization factor irrelevant to further discussion. The complex coefficients $C_{\xi}^m(\phi)$ depend on ionization amplitudes, and the index ξ denotes the ionization path. For one-photon ionization $\xi = \ell_{\xi}$, where ℓ_{ξ} is the orbital momentum of the photoelectron with possible values $\ell_{\xi} = s, d$. For two-photon ionization $\xi = \{\ell_{\xi}, \ell'_{\xi}\}$, where ℓ'_{ξ} is the orbital momentum of the virtual intermediate state, with possible combinations $\xi = ps, pd, fd$.

After applying the Wigner-Eckart theorem (39) to factor out the dependence on the projection m , the nonvanishing coefficients $C_{\xi}^m(\phi)$ may be expressed as (for brevity, we omit the argument ϕ when writing the coefficients):

$$C_s^0 = -\frac{1}{\sqrt{3}} D_s e^{i\phi}, \quad C_d^0 = \sqrt{\frac{2}{15}} D_d e^{i\phi}, \quad C_d^{\pm 1} = \frac{1}{\sqrt{10}} D_d e^{i\phi}, \quad (\text{S9})$$

$$\begin{aligned}
C_{ps}^0 &= -\frac{1}{3}D_{ps}, & C_{pd}^0 &= -\frac{2}{15}D_{pd}, & C_{pd}^{\pm 1} &= -\frac{1}{10}D_{pd}, \\
C_{fd}^0 &= \frac{\sqrt{2}}{5\sqrt{7}}D_{fd}, & C_{fd}^{\pm 1} &= \frac{2}{5\sqrt{21}}D_{fd}.
\end{aligned} \tag{S10}$$

Here

$$D_\xi = d_\xi e^{i\eta_\xi} \tag{S11}$$

are complex reduced matrix elements, independent of m with the absolute value

$$d_\xi = |D_\xi|. \tag{S12}$$

and phase η_ξ . Note that one- (first order) and two-photon (second order) matrix elements (S11), both marked by a single index ξ , are proportional to the square root of intensity, and intensity of the field, respectively. Explicit expressions for D_ξ are presented below.

Equation (S8) can be readily cast into the form (S3), where

$$A_0(E_k) = \frac{I_0}{4\pi} \sum_{\lambda=\text{even}} Z_\lambda P_\lambda(\cos \theta), \quad A(E_k) = \frac{I_0}{4\pi} N, \tag{S13}$$

$$\cos \Delta\eta(E_k) = N^{-1} \sum_{\lambda=\text{odd}} \text{Re} Z'_\lambda P_\lambda(\cos \theta), \tag{S14}$$

$$\sin \Delta\eta(E_k) = N^{-1} \sum_{\lambda=\text{odd}} \text{Im} Z'_\lambda P_\lambda(\cos \theta), \tag{S15}$$

$$N = \left| \sum_{\lambda=\text{odd}} Z'_\lambda P_\lambda(\cos \theta) \right|, \tag{S16}$$

and

$$Z_\lambda = \sum_{m=0,\pm 1} \sum_{\xi\bar{\xi}} (-1)^m C_\xi^m C_{\bar{\xi}}^{m*} \sqrt{(2\ell_\xi + 1)(2\ell_{\bar{\xi}} + 1)} (\ell_\xi m, \ell_{\bar{\xi}} - m | \lambda 0) (\ell_\xi 0, \ell_{\bar{\xi}} 0 | \lambda 0), \tag{S17}$$

where $(j_1 m_1, j_2 m_2 | j m)$ are Clebsch-Gordan coefficients (39). The coefficients Z'_λ are expressed also by Eq. (S17), and with the values of C_ξ^m from Eqs. (S9), but omitting the factor $e^{i\phi}$. Equations (S9)-(S17) define $\Delta\eta(E_k)$, provided the reduced matrix elements (S11) are calculated. The intensities of the fundamental and of the second harmonic are factored out in the

coefficients Z'_λ (see Eqs. (S19), (S22) below), therefore they cancel out in Eqs. (S14), (S15) and the phases $\Delta\eta(E_k)$ are independent on the intensities of the harmonics.

Note that the definition of the EWS delay $\Delta\eta(E_k)$ between one- and two-photon ionization implies not less than two ionization channels, which is reflected in the non-vanishing sum over channels in Eq. (S17). Therefore, the EWS delay is always angle-dependent in contrast to the case of pure one-photon ionization: the EWS delay for an isotropic initial state and isotropic residual ion is independent of the emission angle θ (40, 41). For pure one-photon or pure two-photon ionization in which one channel has negligible amplitude, the EWS time delay may also be isotropic.

The reduced matrix element of the Ne one-photon $2p$ -ionization in first order perturbation theory can be cast in the conventional form (38)

$$D_\ell = i^{-\ell} e^{i\delta_\ell} A_\ell, \quad (\text{S18})$$

$$A_\ell = \sqrt{3}(10, 10 | \ell 0) \sqrt{I_{2\omega}} \int_0^\infty r^3 dr R_{E_k \ell}(r) R_{2p}(r), \quad (\text{S19})$$

where $R_{2p}(r)$ and $R_{E_k \ell}(r)$ are, respectively, the radial wave functions of the $2p$ electron and of the photoelectron with orbital momentum ℓ and energy E_k . The latter is real and possesses the asymptotic form

$$R_{E_k \ell}(r) = \frac{1}{\sqrt{\pi k}} \sin \left(kr - \frac{\ell\pi}{2} - \frac{1}{k} \ln 2kr + \delta_\ell \right), \quad (\text{S20})$$

δ_ℓ is the scattering phase, and $k = \sqrt{E_k} \text{ Ry}^{1/2}$. Furthermore, the second order reduced matrix element is of the form

$$D_{\ell\ell'} = i^{-\ell} e^{i\delta_\ell} A_{\ell,\ell'} \quad (\text{S21})$$

$$A_{\ell,\ell'} = \sqrt{3(2\ell' + 1)}(10, 10 | \ell' 0)(\ell' 0, 10 | \ell 0) \times I_\omega \sum_n \int r'^3 dr' r^3 dr \frac{R_{E_k \ell}(r') R_{n\ell'}(r') R_{n\ell'}(r) R_{2p}(r)}{E_{2p} - E_n + \omega}, \quad (\text{S22})$$

where the summation/integration is over the unoccupied neon electronic states with energies E_n , radial wave functions $R_{n\ell'}$ and orbital momentum ℓ' . Note that A_ℓ and $A_{\ell,\ell'}$ both have

dimensions of [Energy]^{1/2} With our definitions in (S9)-(S11):

$$\eta_\ell = \begin{cases} \delta_\ell - \frac{\ell\pi}{2} & \text{for } A_\ell \geq 0, \\ \delta_\ell - \frac{\ell\pi}{2} + \pi & \text{for } A_\ell < 0 \end{cases}. \quad (\text{S23})$$

and similarly,

$$\eta_{\ell\ell'} = \begin{cases} \delta_\ell - \frac{\ell\pi}{2} & \text{for } A_{\ell\ell'} \geq 0, \\ \delta_\ell - \frac{\ell\pi}{2} + \pi & \text{for } A_{\ell\ell'} < 0 \end{cases}. \quad (\text{S24})$$

Our model for calculations of the first- and second-order ionization amplitudes in neon, the latter by the variationally stable method of infinite summation over the intermediate states in Eq. (S22) (42–44), was described and used recently in (45).

Fig. 2 in the main text depicts phase shift differences $\Delta\eta$ of two-photon ionization relative to one-photon ionization calculated by the recipe described above, as a function of the polar angle θ and photoelectron kinetic energy, while Fig. S1 depicts the corresponding EWS delay differences $\Delta\tau$ defined by Eq. (S4).

Real-time *ab initio* simulations

Method

We numerically simulated the photoionization of Ne irradiated by two-color XUV pulses, using the time-dependent complete-active-space self-consistent field (TD-CASSCF) method (46, 47). The dynamics of the laser-driven multielectron system is described by the time-dependent Schrödinger equation (TDSE),

$$i\frac{\partial\Psi(t)}{\partial t} = \hat{H}(t)\Psi(t), \quad (\text{S25})$$

where the time-dependent Hamiltonian is

$$\hat{H}(t) = \hat{H}_1(t) + \hat{H}_2, \quad (\text{S26})$$

with the one-electron part,

$$\hat{H}_1(t) = \sum_i \hat{h}(\mathbf{r}_i, t) \quad (\text{S27})$$

and the two-electron part,

$$\hat{H}_2 = \sum_{i=1}^N \sum_{j<i} \frac{1}{|\mathbf{r}_i - \mathbf{r}_j|}. \quad (\text{S28})$$

We employ the velocity gauge for the laser-electron interaction in the one-body Hamiltonian:

$$\hat{h}(\mathbf{r}, t) = \frac{\hat{\mathbf{p}}^2}{2} + \mathbf{A}(t) \cdot \hat{\mathbf{p}} - \frac{Z}{|\mathbf{r}|}, \quad (\text{S29})$$

where $\mathbf{A}(t) = -\int \mathbf{E}(t) dt$ is the vector potential, and $\mathbf{E}(t)$ is the laser electric field, see Eq.(2) in the main text, and Z (=10 for Ne) the atomic number.

In the TD-CASSCF method, the total electronic wave function is given in the configuration interaction (CI) expansion,

$$\Psi(\vec{x}_1, \vec{x}_2, \dots, \vec{x}_N, t) = \sum_I C_I(t) \Phi_I(\vec{x}_1, \vec{x}_2, \dots, \vec{x}_N, t). \quad (\text{S30})$$

where \vec{x} is a set of a spin coordinates σ and spatial coordinates \vec{r} . The electronic configuration $\Phi_I(\vec{x}_1, \vec{x}_2, \dots, \vec{x}_N, t)$ is a Slater determinant composed of spin orbital functions $\{\psi_p(\vec{r}, t) \times s(\sigma)\}$, where $\{\psi_p(\vec{r}, t)\}$ and $\{s(\sigma)\}$ denote spatial orbitals and spin functions, respectively. Both the CI coefficients $\{C_I\}$ and orbitals vary in time.

The TD-CASSCF method classifies the spatial orbitals into three groups: doubly occupied and time-independent frozen core (FC), doubly occupied and time-dependent dynamical core (DC), and fully correlated active orbitals:

$$\Psi = \hat{A} \left[\Phi_{\text{fc}} \Phi_{\text{dc}} \sum_I \Phi_I C_I \right], \quad (\text{S31})$$

where \hat{A} denotes the antisymmetrization operator, Φ_{fc} and Φ_{dc} the closed-shell determinants formed with numbers n_{fc} FC orbitals and n_{dc} DC orbitals, respectively, and $\{\Phi_I\}$ the determinants constructed from n_{a} active orbitals. We consider all the possible distributions of active electrons among active orbitals. Thanks to this decomposition, we can significantly reduce the computational cost without sacrificing the accuracy in the description of correlated multi-electron dynamics. The equations of motion that describe the temporal evolution of the CI

coefficients $\{C_I\}$ and the orbital functions $\{\psi_p\}$ are derived by use of the time-dependent variational principle (46). The numerical implementation of the TD-CASSCF method for atoms is detailed in Refs. (47, 48).

Extraction of the photoelectron angular distribution and the phase shift difference

From the obtained time-dependent wave functions, we extract the angle-resolved photoelectron energy spectrum (ARPES) by use of the time-dependent surface flux (tSURFF) method (49). This method computes the ARPES from the electron flux through a surface located at a certain radius R_s , beyond which the outgoing flux is absorbed by the infinite-range exterior complex scaling (48, 50).

We introduce the time-dependent momentum amplitude $a_p(\mathbf{k}, t)$ of orbital p for photoelectron momentum \mathbf{k} , defined by,

$$a_p(\mathbf{k}, t) = \langle \chi_{\mathbf{k}}(\mathbf{r}, t) | u(R_s) | \psi_p(\mathbf{r}, t) \rangle \equiv \int_{r > R_s} \chi_{\mathbf{k}}^*(\mathbf{r}, t) \psi_p(\mathbf{r}, t) d^3 \mathbf{r}, \quad (\text{S32})$$

where $\chi_{\mathbf{k}}(\mathbf{r}, t)$ denotes the Volkov wavefunction, and $u(R_s)$ the Heaviside function which is unity for $r > R_s$ and vanishes otherwise. The use of the Volkov wavefunction implies that we neglect the effects of the Coulomb force from the nucleus and the other electrons on the photoelectron dynamics outside R_s , which has been confirmed to be a good approximation (51). The photoelectron momentum distribution $\rho(\mathbf{k})$ is given by,

$$\rho(\mathbf{k}) = \sum_{pq} a_p(\mathbf{k}, \infty) a_q^*(\mathbf{k}, \infty) \langle \Psi(t) | \hat{E}_p^q | \Psi(t) \rangle, \quad (\text{S33})$$

with $\hat{E}_p^q \equiv \sum_{\sigma} \hat{a}_{q\sigma}^\dagger \hat{a}_{p\sigma}$. One obtains $a_p(\mathbf{k}, \infty)$ by numerically integrating,

$$-i \frac{\partial}{\partial t} a_p(\mathbf{k}, t) = \langle \chi_{\mathbf{k}}(t) | [h_s, \theta(R_s)] | \psi_p(t) \rangle + \sum_q a_q(\mathbf{k}, t) \{ \langle \psi_q(t) | \hat{F} | \psi_p(t) \rangle - R_p^q \}, \quad (\text{S34})$$

where $R_p^q = \langle \psi_q | \dot{\psi}_p \rangle - \langle \psi_q | \hat{h} | \psi_p \rangle$, and \hat{F} denotes a nonlocal operator describing the contribution from the inter-electronic Coulomb interaction (47, 48). The numerical implementation of tSURFF to TD-CASSCF is detailed in Ref. (51).

We evaluate the photoelectron angular distribution $I(\theta)$ as a slice of $\rho(\mathbf{k})$ at the value of $|\mathbf{k}|$ corresponding to the photoelectron peak, and as a function of the optical phase ϕ . Then, employing a fitting procedure very similar to that used for the experimental data, we extract the phase shift difference $\Delta\eta$ between one-photon and two-photon ionization at photoelectron energies 7.0 eV, 10.2 eV and 16.6 eV. The results are shown in Fig. 2 in the main text.

References

30. V. Lyamayev, *et al.*, *J. Phys. B* **46**, 164007 (2013).
31. C. Svetina, *et al.*, *J. Synchrotron Rad.* **22**, 538 (2015).
32. B. Diviacco, R. Bracco, D. Millo, M. Musardo, paper presented at IPAC'11, San Sebastian, Spain, September 2009.
33. L. Giannessi, *et al.*, *Sci. Reports* **8**, 7774 (2018).
34. M. Zangrando, *et al.*, *J. Synchrotron Rad.* **22**, 565 (2015).
35. L. Raimondi, *et al.*, *Nucl. Instrum. Meth. A* **710**, 131 (2013).
36. C. Svetina, *et al.*, *J. Synchrotron Rad.* **23**, 35 (2016).
37. V. Dribinski, A. Ossadtchi, V. A. Mandelshtam, H. Reisler, *Rev. Sci. Instrum.* **73**, 2634 (2002).
38. M. Y. Amusia, *Atomic Photoeffect* (New York, London: Plenum, 1990).

39. D. A. Varshalovich, A. N. Moskalev, V. K. Khersonskii, *Quantum Theory Of Angular Momentum* (Singapore: World Scientific, 1988).
40. J. M. Dahlström, E. Lindroth, *J. Phys. B* **47**, 124012 (2014).
41. J. Wätzel, A. S. Moskalenko, Y. Pavlyukh, J. Berakdar, *J. Phys. B* **48**, 025602 (2015).
42. A. Orel, T. Rescigno, *Chem. Phys. Lett.* **146**, 434 (1988).
43. B. Gao, A. F. Starace, *Phys. Rev. A* **39**, 4550 (1989).
44. E. I. Staroselskaya, A. N. Grum-Grzhimailo, *Moscow Univ. Phys. Bull.* **70**, 374 (2015).
45. E. V. Gryzlova, A. N. Grum-Grzhimailo, E. I. Staroselskaya, N. Douguet, K. Bartschat, *Phys. Rev. A* **97**, 013420 (2018).
46. T. Sato, K. L. Ishikawa, *Phys. Rev. A* **88**, 023402 (2013).
47. T. Sato, *et al.*, *Phys. Rev. A* **94**, 023405 (2016).
48. Y. Orimo, T. Sato, A. Scrinzi, K. L. Ishikawa, *Phys. Rev. A* **97**, 023423 (2018).
49. L. Tao, A. Scrinzi, *New J. Phys.* **14**, 013021 (2012).
50. A. Scrinzi, *Phys. Rev. A* **81**, 053845 (2010).
51. Y. Orimo, T. Sato, K. L. Ishikawa, <https://arxiv.org/abs/1903.10743v2> (2019).
52. C. Palatchi, J. M. Dahlström, A. S. Kheifets, I. A. Ivanov, D. M. Canaday, P. Agostini, L. F. DiMauro, *J. Phys. B* **47**, 245003 (2014)
53. D. Guénot, D. Kroon, E. Balogh, E. W. Larsen, M. Kotur, M. Miranda, T. Fordell, P. Johnson, J. Mauritsson, M. Gisselbrecht, K. Varjú, C. L. Arnold, T. Carette, A. S. Kheifets, E. Lindroth, A. L'Huillier, J. M. Dahlström, *J. Phys. B* **47**, 245602, (2014).

54. M. Di Fraia *et al.*, submitted for publication.

Table S1. Table of experimental parameters. E_k is the kinetic energy of the photoelectrons. Transmission takes account of reflection and geometric losses.

$\hbar\omega$, eV	E_k , eV	Pulse energy, μJ (exit undulator)	Transmission	Pulse energy, μJ (exp. station)	Average irradiance W/cm^2
14.3	7.0	45	0.16	7.2	3.6×10^{14}
15.9	10.2	95	0.20	19	1.0×10^{15}
19.1	16.6	84	0.29	24.4	1.2×10^{15}

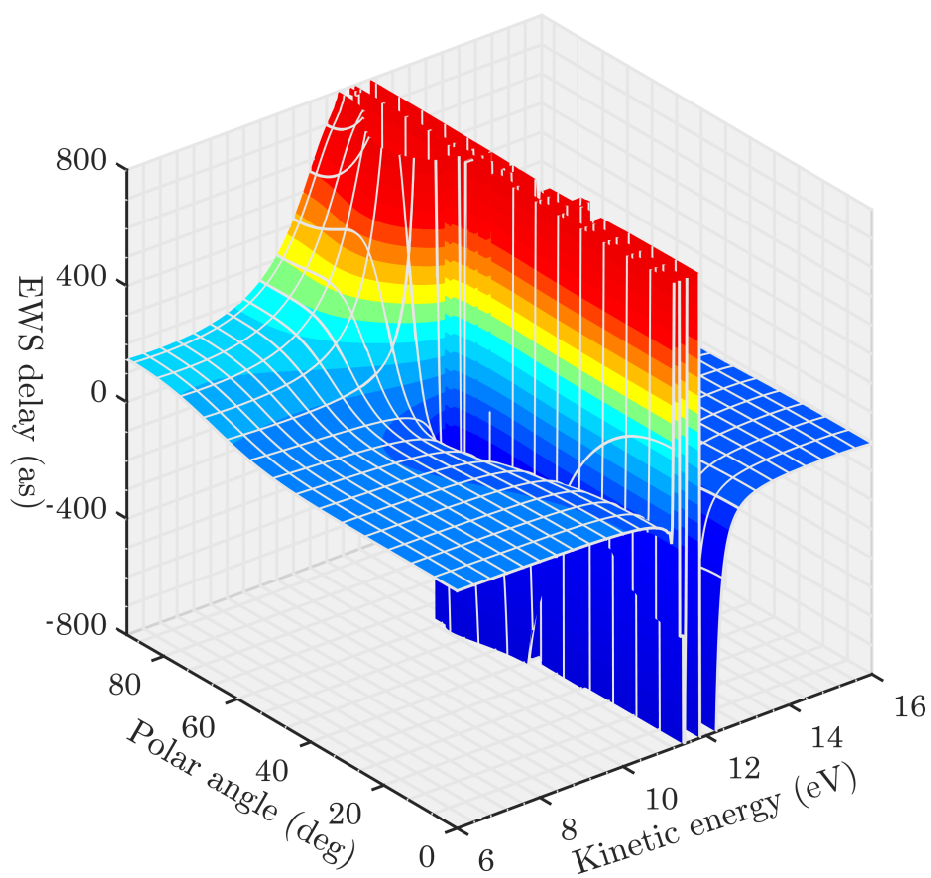


Fig. S1. Calculated EWS delay differences $\Delta\tau$ of two-photon ionization relative to one-photon ionization as a function of the polar angle θ and photoelectron kinetic energy below the $2p \rightarrow 3s$ resonance at 12.0 eV kinetic energy.